

A Pressure Responsive Artificial Interphase Layer of BaTiO₃ against Dendrite Growth for Stable Lithium Metal Anodes

Zhuo Li⁺^[a] Rui Yu⁺^[a] Siwei Gui,^[b] Hui Yang,^{*[b]} and Xin Guo^{*[a]}

Development of lithium (Li) metal anodes in high-energy-density batteries is considerably impeded by uncontrolled dendrite growth, side reactions, and related volume changes. In this work, a pressure responsive artificial interphase layer of piezoelectric BaTiO₃ (BTO) is constructed on Li anodes to prevent the formation of Li dendrites. Once protruding Li buds compress the interfacial space, the extruded piezoelectric layer generates an internal electric field to effectively change the local electric field around the bud tips, thus promoting

homogeneous plating/stripping of Li. The artificial interphase layer not only offers a physical protection to the Li anode, but also helps to regulate the Li flux at the Li/electrolyte interface, which then leads to the uniform Li deposition. Consequently, the BTO-protected Li anode exhibits stable cycling and small polarization in both Li||Li and Li||Cu cells. When paired with S, LiFePO₄ and Ni-rich high-voltage cathodes, the Li-metal batteries also exhibit improved cycling stability and high Coulombic efficiency.

Introduction

Metallic lithium (Li) anodes offer the highest theoretical capacity (3860 mAh g⁻¹) and lowest electrochemical potential (-3.04 V vs. standard hydrogen electrode), which have been regarded as the ultimate anode.^[1] Coupled with high-capacity cathodes, such as LiNi_{0.8}Co_{0.1}Mn_{0.1}O₂ (NCM811), Li-metal batteries can realize an ultrahigh specific energy of >500 Wh kg⁻¹, which is much higher than those of current Li-ion batteries.^[2] Additionally, the implementation of metallic Li anodes in lithium-sulfur (Li-S) and lithium-oxygen (Li-O₂) batteries can further promote energy densities to more than 1500 Wh kg⁻¹ (Li-O₂, 3505 Wh kg⁻¹; Li-S, 2600 Wh kg⁻¹).^[3]

However, technical challenges, such as unsatisfactory Coulombic efficiency and uncontrolled dendritic growth, impede the successful deployment of Li-metal batteries.^[4] Spontaneous side reactions of metallic Li with organic electrolytes occur and a thin layer of solid electrolyte interphase (SEI) is formed.^[5] The SEI layer is mechanically unstable, cannot bear the huge volumetric expansion and morphological changes, which causes parasitic reactions between the active Li and the electrolyte, leading to the formation of the "dead" Li and subsequent dendrite growth.^[6]

According to the Li deposition mechanism, Li dendrites favor growth at tips of Li buds under high current densities and capacities (e.g., above the Sand's capacity).^[7] The Li protrusion attracts more Li-ion flux because of the high local electrical field, accelerating the Li deposition onto the tips and the vertical growth of Li dendrites (Figure 1a).^[8] Therefore, it is necessary to inactivate the nucleation sites of Li dendrites as soon as possible to control the nucleation and growth pattern of the Li deposition. Many attempts, including applying solid/polymer electrolytes,^[9] optimizing electrolyte formulae,^[10] employing 3D hosts,^[11] introducing interfacial protective layers,^[12] using composite metal anodes,^[13] and others,^[14] had been made to suppress the dendrite growth; among them, the most effective approach was to construct artificial interphase layers on Li anode surfaces.^[15] Unfortunately, for most artificial interphase layers, the Li-ion migration is much slower than the charge transfer at the Li/electrolyte interface during the Li deposition, creating a Li-ion-deficient layer near the electrode surface and resulting in the growth of Li dendrites.^[16] Some artificial interphase layers cannot accommodate the large volume change during long-term cycling, and are easily destroyed by the interfacial stress/strain.^[17] Up to now, it still faces formidable challenges to achieve dendrite-free Li-metal anodes. To completely prevent the formation of wispy Li dendrites, mossy Li must be inactivated as soon as it firstly appears.^[18]

In this work, we constructed a self-pressure responsive artificial interphase layer of piezoelectric BaTiO₃ (BTO). The piezoelectric interphase layer changed the electric field distribution around tips of nucleated Li buds, regulating Li-ion flux to the Li metal surface, then the Li dendrite growth was effectively prevented by stopping the evolution of the Li buds at the early stage. As a result, the BTO layer-protected Li anode exhibited stable cycling and small polarization in Li||Li and Li||Cu cells, and Li-metal batteries with S, LiFePO₄ and Ni-rich high-voltage cathodes also exhibited significantly improved cycling stability and high Coulombic efficiency.

[a] Dr. Z. Li,⁺ R. Yu,⁺ Prof. X. Guo

State Key Laboratory of Material Processing and Die & Mould Technology

School of Materials Science and Engineering

Huazhong University of Science and Technology

Wuhan 430074, China

E-mail: xguo@hust.edu.cn

[b] S. Gui, Prof. H. Yang

Department of Mechanics, School of Aerospace Engineering

Huazhong University of Science and Technology

Wuhan 430074, China

E-mail: huiyang2017@hust.edu.cn

[+] These authors contributed equally to this work.

Supporting information for this article is available on the WWW under <https://doi.org/10.1002/batt.202200142>

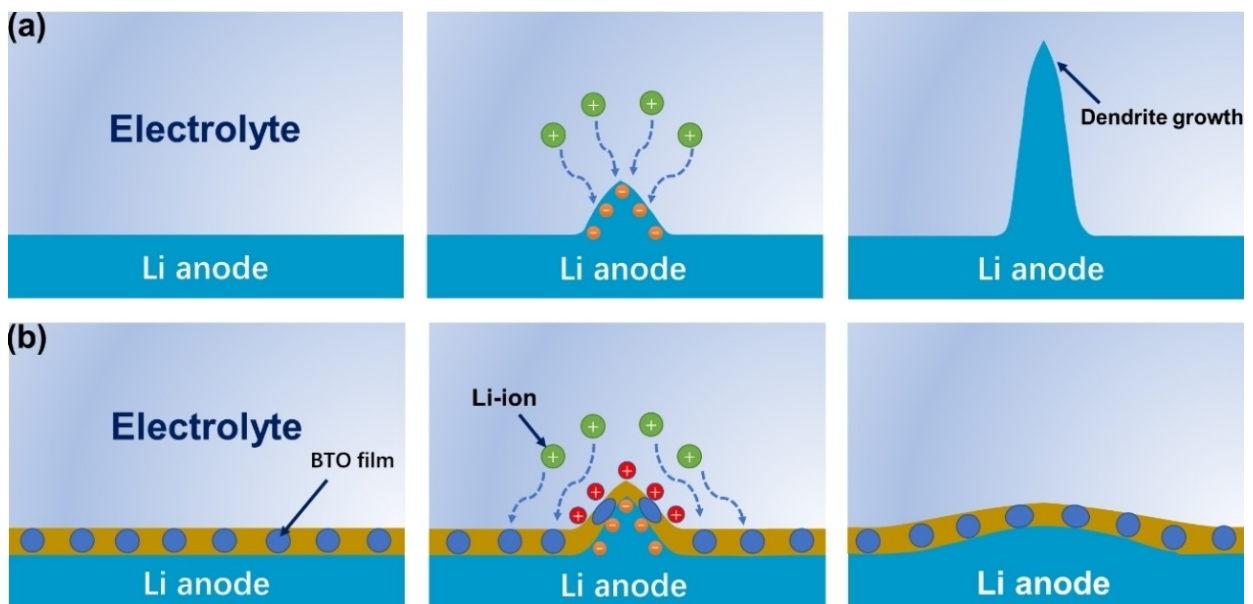


Figure 1. Schematic diagram of the Li plating behavior. a) The “tip effect” attracts more Li-ions due to the enhanced electric field at the tip of a Li bud, leading to fast growth of wispy dendrite. b) Piezoelectric artificial interphase layer changes the electric field around the tip of the Li bud and regulates the Li deposition to keep it homogeneous.

Results and Discussion

Owing to the excellent ferroelectric properties of BTO,^[19] BTO nanoparticles were selected to form the artificial interphase layer. To create a conformal protection layer, the BTO nanoparticles were dispersed in N-methyl pyrrolidone (NMP) with PVDF to form a uniform colloidal solution, which was then casted on the pristine Li/Cu surface via doctor blade. Upon the Li plating/stripping, some tips of the Li buds tend to be formed on the Li anode. Once squeezed by protruding Li buds, the deformed BTO layer effectively decreases the local electric field around the tips of the Li buds, and instantaneously creates positive and negative charges on their upper and lower surfaces, respectively. The decreased electric field and positive charges on top of the upper surface promote the subsequent Li deposition at the root of the Li tips rather than in the stress center, thereby reducing the effective current density and homogenizing the ion flux near the Li anode surface, which further suppresses the dendrite growth in the vertical direction at initial stage (Figure 1b). Therefore, the multifunctional BTO layer can not only act as a robust protective layer to the Li anode, but also decrease the electric field around the tips, thus leading to a dendrite-free and stable electrochemical interface.

To verify the polarization in the BTO layer, X-Ray diffraction (XRD) patterns were obtained; result (Figure S1) indicated a ferroelectric tetragonal (*t*-BTO) phase in the BTO layer.^[20] The scanning electron microscopy (SEM) image (Figure S2) showed a uniform distribution of the BTO nanoparticles with an average size of ~90 nm. According to the cross-view of SEM image (Figure S3), the thickness of the BTO layer was ~8 μm. Afterward, ferroelectric properties of the BTO layer were investigated by the piezoelectric force microscopy (PFM); the BTO layer showed a rectangle-like hysteresis loop with a sharply modu-

lated phase (Figure S4). Such polarized transformation confirmed excellent ferroelectric properties of the BTO layer.

To investigate roles of the BTO layer in suppressing the growth of the dendritic Li and stabilizing the Li anode, Li@BTO||Li@BTO and Li||Li symmetric cells were assembled and tested at a rate of 1 mA cm⁻² (capacity: 1 mAh cm⁻²). 1 M lithium bis(trifluoromethanesulfonyl)imide (LiTFSI) in dioxolane/dimethoxyethane (DOL/DME) (1:1 in volume) with 1% LiNO₃ was adopted as the electrolyte. As shown in Figure 2a, the polarization of the Li@BTO||BTO@Li symmetric cell slightly decreased in initial cycles and tended to be stable after 100 h. Moreover, the cell with Li@BTO maintained an almost constant overpotential of 40 mV even after 1000 cycles. In contrast, the symmetric cell with the bare Li anode exhibited a much larger overpotential (over 400 mV) over cycling and finally failed after 400 h, owing to the rapid consumption of Li. Even using a higher capacity (3 mA cm⁻², 6 mAh cm⁻²) and limited Li anode (50 μm in thickness), the Li@BTO||BTO@Li cell hold a stable cycling for over 200 h, while the Li||Li cell showed a large polarization after 25 h (Figure S5 in the Supporting Information).

Furthermore, the Li@BTO||BTO@Li cell showed an excellent rate performance (Figure S6, Supporting Information). With increasing current, the Li@BTO symmetric cell delivered low overpotential and stable voltage oscillations, indicating a stable and dendrite-free Li anode. However, the symmetric Li||Li cell suffered from a serious voltage fluctuation. As the current density increased to 6 mA cm⁻², the Li@BTO||BTO@Li cell still maintained a stable cycling, while the symmetric Li||Li cell showed a micro-short-circuit. When the electrical current went back to 1 mA cm⁻², the overvoltage of the Li@BTO||BTO@Li cell recovered to its initial value, demonstrating good reversibility.

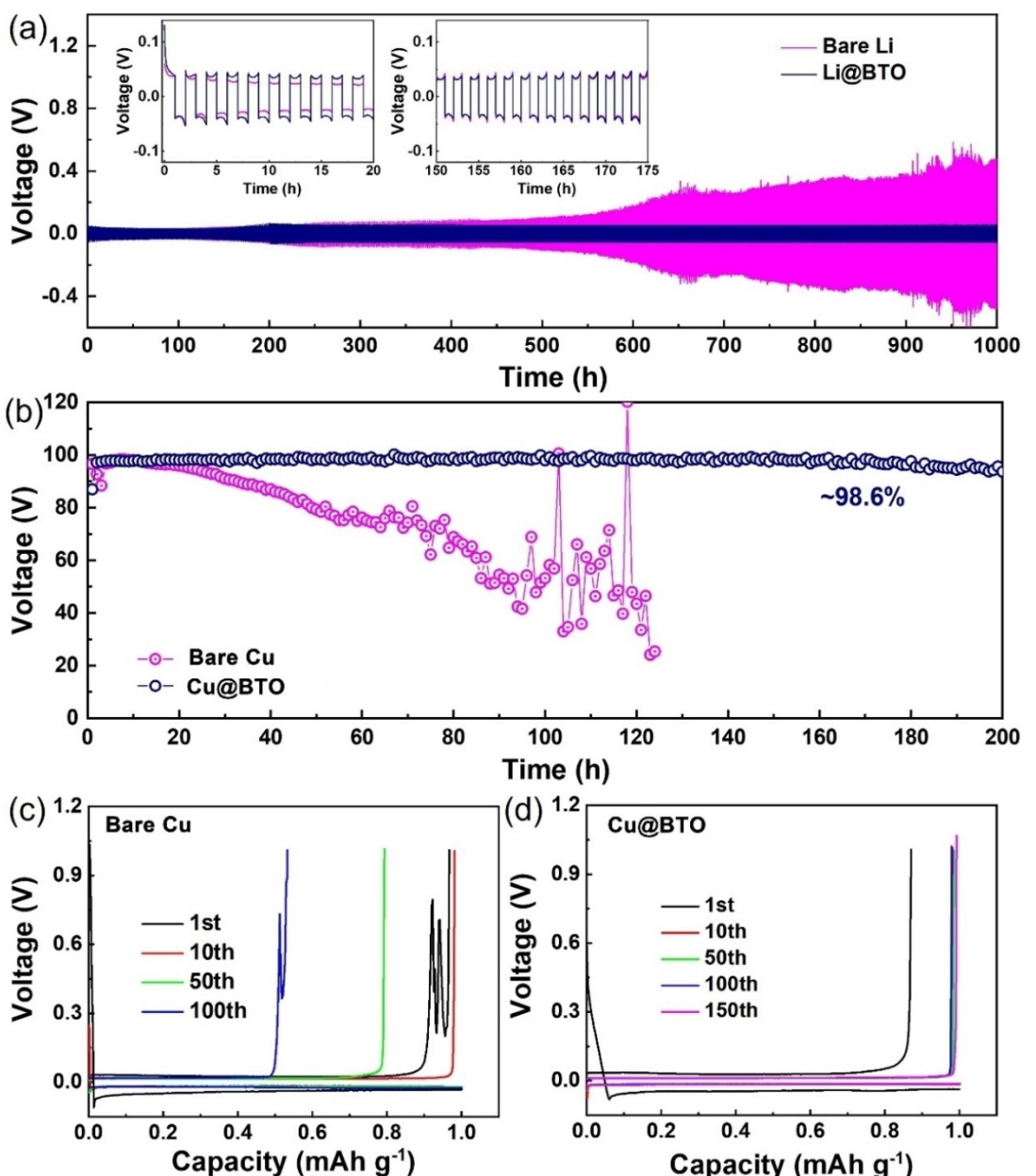


Figure 2. Electrochemical properties of Li anodes with or without the piezoelectric artificial interphase layer. a) Tests of symmetric cells of Li@BTO and bare Li at a current density of 1 mA cm^{-2} (1 mAh cm^{-2}), inset: the blow-up of voltage profiles during 0 to 20 h and 150 to 175 h. b) Coulombic efficiency of Li plating/stripping in $\text{Li} \parallel \text{Cu}$ cells using different Cu working electrodes. Voltage profiles for the Li plating/stripping on different Cu working electrodes at a current density of 1 mA cm^{-2} ; c) bare Cu, d) BTO@Cu. Li was electro-deposited at 1 mA cm^{-2} to a total capacity of 1 mAh cm^{-2} , followed by stripping to a cut-off voltage of 1.0 V vs. Li^+/Li .

In these symmetric cells, the overpotential for the Li plating in the Li@BTO symmetric cell was much higher than that in the symmetric $\text{Li} \parallel \text{Li}$ cell during first few cycles, mainly due to the poor electrical conductivity of the BTO layer before the layer was completely wetted by the electrolyte. Then, the overpotential of the Li@BTO symmetric cell decreased to levels lower than that of the bare Li cell after initial dozens of cycles. Subsequently, we employed the electrochemical impedance spectroscopy (EIS) measurements to investigate the interfacial changes in the two symmetric cells at different states (Figures S7, Supporting Information). The Li@BTO symmetric

cell had higher initial bulk and interfacial resistance; interestingly, after cycling, both the bulk and the interfacial resistance of the Li@BTO \parallel BTO@Li symmetric cell became much smaller than those of the symmetric cell with bare Li, verifying the superiority of the BTO layer in facilitating uniform Li deposition.

Coulombic efficiency indicates the Li utilization rate during the Li plating/stripping cycling, and can be calculated by the ratio of the amounts of Li stripped and plated on the working electrode. To investigate the influence of the piezoelectric layer on the Coulombic efficiency of the Li-metal anode, $\text{Li} \parallel \text{Cu}$ and $\text{Li} \parallel \text{Cu@BTO}$ half-cells were tested at a rate of 1 mA cm^{-2} . Upon

cycling, the Li||Cu cell with the bare Li quickly failed in 30 cycles, the Coulombic efficiency decreased to below 40% after 100 cycles (Figure 2b), and the voltage became unstable with a large voltage fluctuation (Figure 2c). On the contrary, the half-cell with the piezoelectric layer maintained a Coulombic efficiency as high as ~98.6% over 200 cycles (Figure 2b). Furthermore, the overpotential of the Li||Cu@BTO cell held stable at ~22.5 mV for over 200 cycles (Figure 2d).

We employed SEM to observe the Li deposition after cycling at a rate of 1 mA cm^{-2} . As shown in Figure 3(a), the top view of the deposited Li exhibited porous structure with

needle-like dendritic Li on the bare Cu surface after cycling, which could be ascribed to the accumulation of uneven Li deposition.^[21] Wispy Li dendrites rapidly consumed the electrolyte and/or the bulk Li during the long-term cycling because of the repeated break/repair of the SEI layer, which shortened the cycle lifespan of the cell.^[22] In contrast, the deposited Li morphology was highly flat and dense without bulges and pits when the piezoelectric layer was used (Figure 3b). As a result, the Li nuclei showed spherical morphology and compact stacking. Additionally, the surface of the deposited Li still remained smooth with metallic luster, as compared with that of

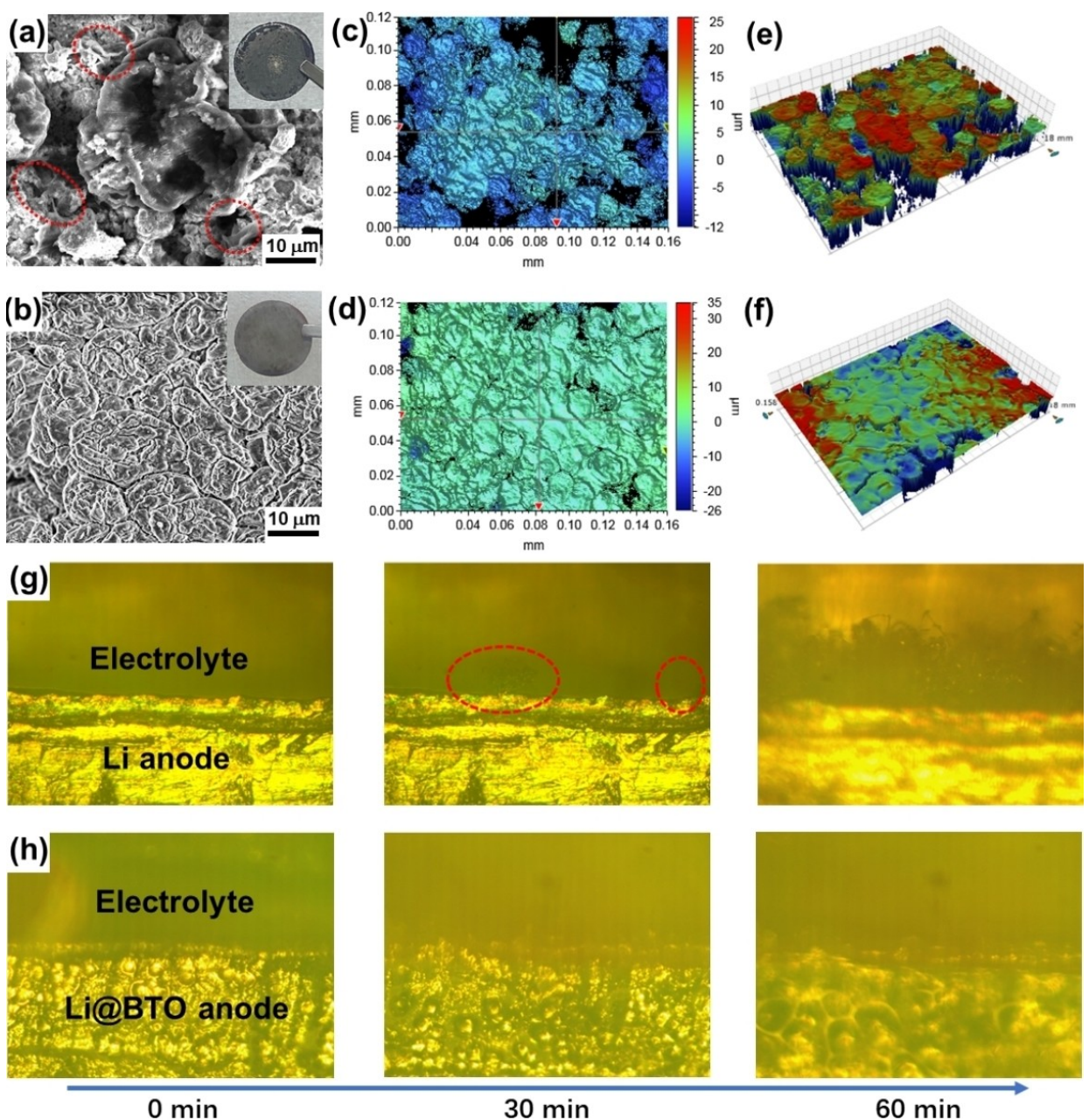


Figure 3. Characterizations of the Li deposition with or without the piezoelectric artificial interphase layer. Top-view SEM images and corresponding digital photographs of the Li deposition on different Cu electrodes: a) bare Cu, b) Cu@BTO. The 2D and 3D AFM morphologies of the Li deposition on different Cu electrodes: c, e) bare Cu; d, f) Cu@BTO. In-situ observations of the Li deposition behavior at a current density of 2 mA cm^{-2} with different Li anodes: g) bare Li, h) Li@BTO.

the bare Cu electrode (insets in Figure 2a and b), revealing that the Li dendritic growth was effectively suppressed by the BTO layer. The cross-sectional SEM images in Figure S8 reveal a uniform surface of Cu@BTO, while non-uniform profiles and “dead” Li could be clearly found on the cycled bare Cu electrode. Moreover, the cycled Cu@BTO exhibited a densely deposited Li layer underneath the BTO layer with an average thickness of ~16.8 μm , while the thickness of the Li deposition layer on the bare Cu was ~29 μm because of the loose and porous structure. We further characterized the Li deposition using atomic force microscope (AFM). The morphology of the Li deposited on the bare Cu showed large granular features and cracks (Figure 3c and e). In contrast, the surface of the Li deposited on Cu@BTO was smooth and uniform, covered with spherical shell-shaped particles, as shown in Figure 3(d and f). The 2D and 3D topography images observed by AFM were consistent with the SEM investigations. Such spherical shell-shaped deposition geometry was related to the uniform Li deposition. The favorable morphology demonstrated that the piezoelectric layer effectively eliminated the formation and propagation of the Li dendrites, and detrimental side reactions were suppressed as well, which resulted in a long-term cycling stability.

Furthermore, a dedicated cell was assembled to monitor the Li plating/stripping with an optical microscope in real-time and in-situ. At early stage, Li protrusions started to form and served as the Li nucleation sites in the Li||Li cell. After that, uncontrolled proliferation of the Li dendrites spread the entire anode surface, as observed from the side view (Figure 3g). In

contrast, we did not observe any dendritic Li deposition throughout the deposition process in the Li||BTO@Li cell; a more homogeneous nucleation led to compact Li deposition without evolving to detrimental dendritic Li, as shown in Figure 3(h). Therefore, the BTO layer prevented the Li buds from growing into the whisker-like Li dendrites at the early stage, deactivating the Li dendrite growth.

X-ray photoelectron spectroscopy (XPS) was used to analyze the elements and valence on the surface of the Li anodes; results are given in Figure S9. It can be seen that the surface of the Li@BTO anode had a much lower intensities of the CO_3^{2-} peaks^[23] than those of the bare Li anode, indicating less formation of the brittle and poorly ionically conductive Li_2CO_3 .^[24] Additionally, much weaker SO_x peaks^[25] were found on the surface of the cycled Li@BTO. Therefore, the BTO layer suppressed, to a large extent, continuous side-reactions of the active Li with the organic electrolyte.

To validate the Li@BTO anode in actual applications, Li-metal batteries coupling with high-loading LiFePO_4 (LFP) cathodes (mass loading: ~10 mg cm^{-2}) and different Li anodes were assembled and tested; the cycling performances are presented in Figure 4. Both the cells of Li@BTO||LFP and Li||LFP delivered comparable capacity and similar voltage profiles at initial stage (Figure 4a). However, a significantly improved cycling performance was achieved in the Li@BTO||LFP cell (Figure 4b). After 200 cycles, the Li@BTO||LFP cell displayed a capacity retention of 99.1% (~152.7 mAh g^{-1}), whereas the capacity of the Li||LFP cell rapidly decayed after tens of cycles (57%, ~91.2 mAh g^{-1}). The better cycling stability of the

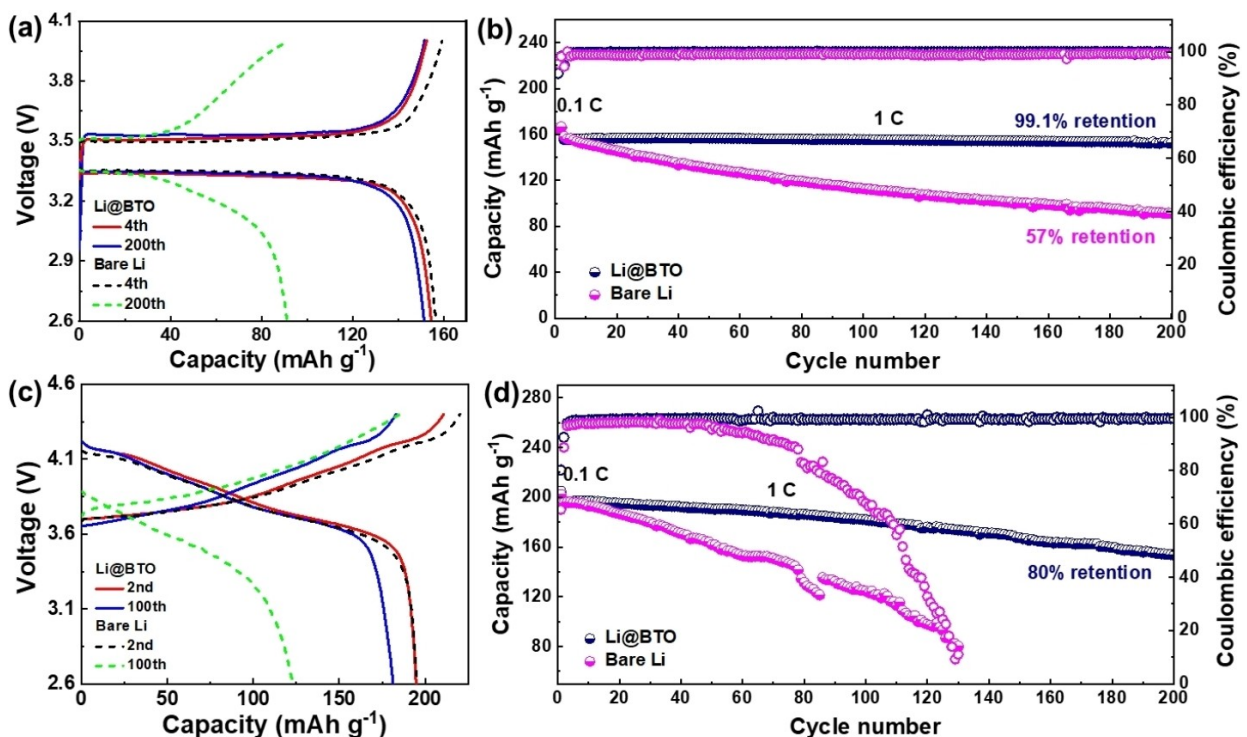


Figure 4. Electrochemical performances of the Li anodes in full cells with different cathodes. a) Typical charge-discharge profiles of the Li@BTO||LFP and Li||LFP cells. b) Cycling performances with corresponding Coulombic efficiency. c) Typical charge-discharge profiles of the Li@BTO||NCM811 and Li||NCM811 cells. d) Cycling performances with corresponding Coulombic efficiency.

Li@BTO||LFP cell was attributed to its stable Li/electrolyte interface, because the piezoelectric BTO layer protected the Li anode.

Li@BTO||S and Li||S cells were also assembled to evaluate the roles of the BTO layer. In Li–S batteries, soluble polysulfide intermediates can shuttle across the separator to react with the Li anode, which severely erodes Li anodes, leading to the fast capacity fading and low Coulombic efficiency.^[26] As shown in Figure S10, the cell with the bare Li had a fast decay in capacity and Coulombic efficiency (below a capacity of 500 mAh g⁻¹, and 90% Coulombic efficiency after 120 cycles). The Li@BTO||S cell, in contrast, showed a prolonged lifespan of more than 200 cycles and the capacity was still above 700 mAh g⁻¹ with a steady Coulombic efficiency of nearly 100%. Therefore, the BTO layer effectively stabilized the surfaces of the Li-metal anode and improved the Coulombic efficiency of the Li||S cell.

A high energy density of $>400 \text{ Wh kg}^{-1}$ is in principle possible for Li-metal batteries with nickel (Ni)-rich high-voltage cathodes of commercial interest.^[27] Unfortunately, Ni-rich cathodes often suffer from a series of bulk and interface degradations, including intergranular cracking of secondary particles, spinel/rock-salt phase transformation, formation and growth of cathode electrolyte interphases (CEIs), and transition metal (TM) dissolution.^[28] Especially, dissolved TMs eventually migrate and precipitate at the anode side and affect the anode stability, leading to the destruction of the SEI and the capacity/voltage decay.^[29]

To evaluate the application of Li@BTO in high-voltage Li-metal batteries with Ni-rich cathode of NCM811, Li||NCM811 batteries were assembled, in which the 1 M lithium hexafluorophosphate in ethylene carbonate and ethyl methyl carbonate (1:1 by volume, abbreviated as 1 M LiPF₆/EC–EMC) was used as the electrolyte. As shown in Figure 4(c), two Li||NCM811 cells, employing the Li@Cu and bare Li anodes, showed similar first-

cycle charge-discharge curves and a discharge capacity of $\sim 196.7 \text{ mAh g}^{-1}$. Upon subsequent cycling, the full cell with the Li@BTO anode presented a higher average Coulombic efficiency and retained $>80\%$ of its initial capacity after 200 cycles, as shown in Figure 4(d). In comparison, the capacity and Coulombic efficiency of the cell with the bare Li showed a cliff-style drop after 75 cycles. Obviously, the SEI formed on the surface of the bare Li anode was too weak to tolerate the attack of TMs, thus triggering Li-electrolyte reactions at the exposed surface. Luckily, the BTO layer not only suppressed the growth of the Li dendrites, but also prevented the destruction of TMs.

To better understand how the BTO layer influenced the Li deposition behavior, finite element simulations were conducted with COMSOL Multiphysics. By solving the Laplace equation,^[30] the current density distributions around a newly nucleated Li bud with or without the BTO layer were analyzed to elucidate the effect of the BTO layer on regulating the Li-ion flux around the Li bud; corresponding simulation details are provided in the Supporting Information Figure S11. Figure 5(a) shows the current density distribution around a Li bud on the bare Li anode. The tip of the Li bud experienced the highest current density, indicating fast Li-ion flux onto the tip, which promoted uneven Li deposition and vertical dendrite growth. However, in the presence of the BTO layer, a piezoelectric potential was established and the current (Li-ion flux) near the tip region of the Li bud was highly suppressed, leading to the Li deposition on lateral sides of the Li bud until a flat deposition layer was formed (Figure 5b).

Conclusion

The piezoelectric BTO layer created an internal electric field via the self-pressure response to significantly decrease the local

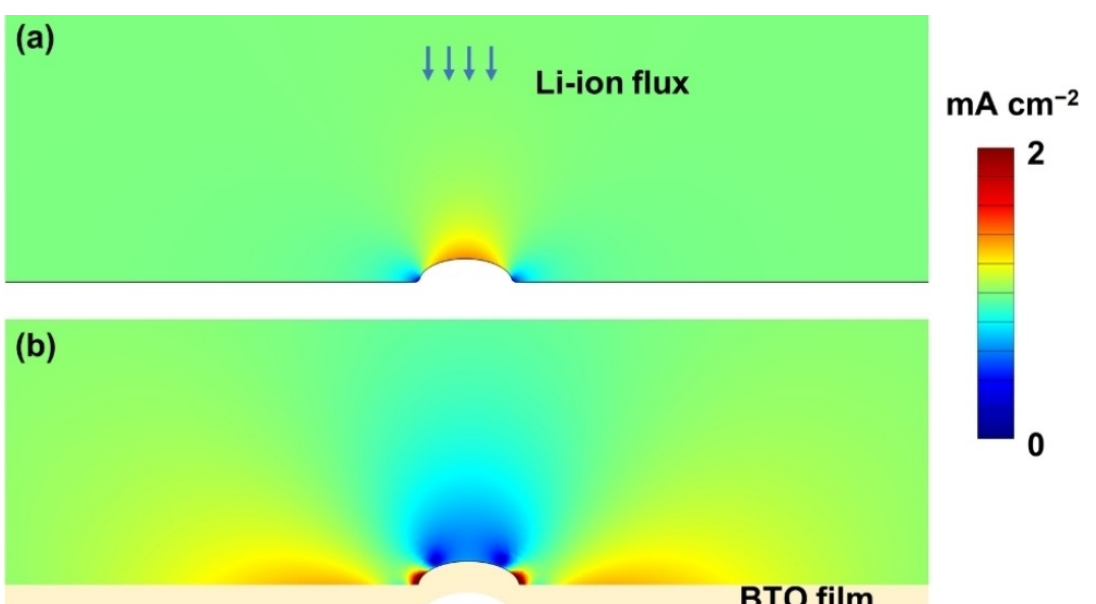


Figure 5. Finite element simulations of the current density distributions around a newly nucleated Li bud on different Li anodes: a) bare Li anode, b) Li@BTO anode.

electric field intensity, which acted as spatial conformation of the Li tips; consequently, the tips of the Li buds were leveled out. Therefore, the Li dendrite growth was effectively prevented by the BTO layer, and the outstanding electrochemical performances of Li-metal batteries were achieved. Under the protection of the BTO layer, the Li@BTO anode enabled superior cycling stability in the Li-metal batteries with S, LiFePO₄, and Ni-rich high-voltage cathodes. Such a piezoelectric layer is also applicable to the design of SEI for Na and Zn metal anodes.

Acknowledgements

The authors would like to express their appreciation to the National Natural Science Foundation of China and the Israeli Science Foundation for funding this research within the framework of the joint NSFC-ISF Grant#51961145302. This work is also supported by the National Natural Science Foundation of China (Grant#12172143) and China Postdoctoral Science Foundation funded project (Grant#2020M682403). The analytical and testing center of Huazhong University of Science and Technology is acknowledged for the SEM and XPS investigations.

Conflict of Interest

The authors declare no conflict of interest.

Data Availability Statement

The data that support the findings of this study are available from the corresponding author upon reasonable request.

Keywords: artificial interphase layer • current density distribution • lithium dendrites • lithium metal anode • rechargeable batteries

- [1] a) B. Liu, J.-G. Zhang, W. Xu, *Joule* **2018**, *2*, 833–845; b) J. Zheng, M. H. Engelhard, D. Mei, S. Jiao, B. J. Polzin, J.-G. Zhang, W. Xu, *Nat. Energy* **2017**, *2*, 17012.
- [2] a) W. Xue, M. Huang, Y. Li, Y. G. Zhu, R. Gao, X. Xiao, W. Zhang, S. Li, G. Xu, Y. Yu, P. Li, J. Lopez, D. Yu, Y. Dong, W. Fan, Z. Shi, R. Xiong, C.-J. Sun, I. Hwang, W.-K. Lee, Y. Shao-Horn, J. A. Johnson, J. Li, *Nat. Energy* **2021**, *6*, 495–505; b) D. Lin, Y. Liu, Y. Cui, *Nat. Nanotechnol.* **2017**, *12*, 194–206.
- [3] a) E. Cha, M. D. Patel, J. Park, J. Hwang, V. Prasad, K. Cho, W. Choi, *Nat. Nanotechnol.* **2018**, *13*, 337–344; b) W. J. Kwak, Rosy, D. Sharon, C. Xia, H. Kim, L. R. Johnson, P. G. Bruce, L. F. Nazar, Y. K. Sun, A. A. Frimer, M. Noked, S. A. Freunberger, D. Aurbach, *Chem. Rev.* **2020**, *120*, 6626–6683; c) J. Yi, Y. Liu, Y. Qiao, P. He, H. Zhou, *ACS Energy Lett.* **2017**, *2*, 1378–1384; d) J. I. Lee, G. Song, S. Cho, D. Y. Han, S. Park, *Batteries & Supercaps* **2020**, *3*, 828–859.
- [4] a) X. Gao, Y.-N. Zhou, D. Han, J. Zhou, D. Zhou, W. Tang, J. B. Goodenough, *Joule* **2020**, *4*, 1864–1879; b) R. Wang, W. Cui, F. Chu, F. Wu, *J. Energy Chem.* **2020**, *48*, 145–159.
- [5] a) X. B. Cheng, R. Zhang, C. Z. Zhao, Q. Zhang, *Chem. Rev.* **2017**, *117*, 10403–10473; b) X. Cheng, F. Xian, Z. Hu, C. Wang, X. Du, H. Zhang, S. Chen, S. Dong, G. Cui, *Angew. Chem. Int. Ed. Engl.* **2019**, *58*, 5936–5940.
- [6] a) Y. Liu, D. Lin, P. Y. Yuen, K. Liu, J. Xie, R. H. Dauskardt, Y. Cui, *Adv. Mater.* **2017**, *29*, 1605531; b) N. W. Li, Y. X. Yin, C. P. Yang, Y. G. Guo, *Adv. Mater.* **2016**, *28*, 1853–1858.
- [7] P. Bai, J. Li, F. R. Brushett, M. Z. Bazant, *Energy Environ. Sci.* **2016**, *9*, 3221–3229.
- [8] a) W. Zhang, H. L. Zhuang, L. Fan, L. Gao, Y. Lu, *Sci. Adv.* **2018**, *4*, eaar4410 ; b) X. Zhang, Y. Yang, Z. Zhou, *Chem. Soc. Rev.* **2020**, *49*, 3040–3071.
- [9] a) Z. Li, X.-Y. Zhou, X. Guo, *Energy Storage Mater.* **2020**, *29*, 149–155; b) Z. Li, H. M. Huang, J. K. Zhu, J. F. Wu, H. Yang, L. Wei, X. Guo, *ACS Appl. Mater. Interfaces* **2019**, *11*, 784–791; c) Z. Li, J. Fu, S. G. Zheng, D. Li, X. Guo, *Small* **2022**, *18*, 2200891.
- [10] a) X. Cao, X. Ren, L. Zou, M. H. Engelhard, W. Huang, H. Wang, B. E. Matthews, H. Lee, C. Niu, B. W. Arey, Y. Cui, C. Wang, J. Xiao, J. Liu, W. Xu, J.-G. Zhang, *Nat. Energy* **2019**, *4*, 796–805; b) X. Fan, L. Chen, O. Borodin, X. Ji, J. Chen, S. Hou, T. Deng, J. Zheng, C. Yang, S. C. Liou, K. Amine, K. Xu, C. Wang, *Nat. Nanotechnol.* **2018**, *13*, 715–722; c) Q. Zheng, Y. Yamada, R. Shang, S. Ko, Y.-Y. Lee, K. Kim, E. Nakamura, A. Yamada, *Nat. Energy* **2020**, *5*, 291–298; d) C. Yan, Y. X. Yao, X. Chen, X. B. Cheng, X. Q. Zhang, J. Q. Huang, Q. Zhang, *Angew. Chem. Int. Ed. Engl.* **2018**, *57*, 14055–14059; e) X. Q. Zhang, T. Li, B. Q. Li, R. Zhang, P. Shi, C. Yan, J. Q. Huang, Q. Zhang, *Angew. Chem. Int. Ed. Engl.* **2020**, *59*, 3252–3257.
- [11] C. P. Yang, Y. X. Yin, S. F. Zhang, N. W. Li, Y. G. Guo, *Nat. Commun.* **2015**, *6*, 8058.
- [12] a) Z. Wang, Y. Wang, Z. Zhang, X. Chen, W. Lie, Y. B. He, Z. Zhou, G. Xia, Z. Guo, *Adv. Funct. Mater.* **2020**, *30*, 2002414; b) L. Yang, Y. Song, H. Liu, Z. Wang, K. Yang, Q. Zhao, Y. Cui, J. Wen, W. Luo, F. Pan, *Small Methods* **2020**, *4*, 1900751; c) S. Zheng, H. Zhang, J. Fan, Q. Xu, Y. Min, *Small* **2021**, *17*, 2102347.
- [13] a) Y. Fang, R. Lian, H. Li, Y. Zhang, Z. Gong, K. Zhu, K. Ye, J. Yan, G. Wang, Y. Gao, Y. Wei, D. Cao, *ACS Nano* **2020**, *14*, 8744–8753; b) Y. Fang, Y. Zhang, K. Zhu, R. Lian, Y. Gao, J. Yin, K. Ye, K. Cheng, J. Yan, G. Wang, Y. Wei, D. Cao, *ACS Nano* **2019**, *13*, 14319–14328.
- [14] Y. Gao, F. Qiao, J. You, C. Shen, H. Zhao, J. Gu, Z. Ren, K. Xie, B. Wei, *J. Energy Chem.* **2021**, *55*, 580–587.
- [15] a) T. Wang, Y. Hua, Z. Xu, J. S. Yu, *Small* **2022**, *18*, 2102250; b) Z. Han, C. Zhang, Q. Lin, Y. Zhang, Y. Deng, J. Han, D. Wu, F. Kang, Q.-H. Yang, W. Lv, *Small Methods* **2021**, *5*, 2001035.
- [16] a) R. Xu, X.-B. Cheng, C. Yan, X.-Q. Zhang, Y. Xiao, C.-Z. Zhao, J.-Q. Huang, Q. Zhang, *Matter* **2019**, *1*, 317–344; b) D. Kang, M. Xiao, J. P. Lemmon, *Batteries & Supercaps* **2020**, *4*, 445–455.
- [17] a) J. Xiang, Z. Cheng, Y. Zhao, B. Zhang, L. Yuan, Y. Shen, Z. Guo, Y. Zhang, J. Jiang, Y. Huang, *Adv. Sci.* **2019**, *6*, 1901120; b) N. W. Li, Y. Shi, Y. X. Yin, X. X. Zeng, J. Y. Li, C. J. Li, L. J. Wan, R. Wen, Y. G. Guo, *Angew. Chem. Int. Ed. Engl.* **2018**, *57*, 1505–1509.
- [18] a) T. Wang, Y. Li, J. Zhang, K. Yan, P. Jaumaux, J. Yang, C. Wang, D. Shanmukaraj, B. Sun, M. Armand, Y. Cui, G. Wang, *Nat. Commun.* **2020**, *11*, 5429; b) Z. Ju, J. Nai, Y. Wang, T. Liu, J. Zheng, H. Yuan, O. Sheng, C. Jin, W. Zhang, Z. Jin, H. Tian, Y. Liu, X. Tao, *Nat. Commun.* **2020**, *11*, 488.
- [19] a) L. Wang, R. Xie, B. Chen, X. Yu, J. Ma, C. Li, Z. Hu, X. Sun, C. Xu, S. Dong, T. S. Chan, J. Luo, G. Cui, L. Chen, *Nat. Commun.* **2020**, *11*, 5889; b) S. Xia, Y. Zhao, J. Yan, J. Yu, B. Ding, *ACS Nano* **2021**, *15*, 3161–3170.
- [20] B. Han, D. Feng, S. Li, Z. Zhang, Y. Zou, M. Gu, H. Meng, C. Wang, K. Xu, Y. Zhao, H. Zeng, C. Wang, Y. Deng, *Nano Lett.* **2020**, *20*, 4029–4037.
- [21] X. Liang, Q. Pang, I. R. Kochetkov, M. S. Sempere, H. Huang, X. Sun, L. F. Nazar, *Nat. Energy* **2017**, *2*, 228462.
- [22] a) J. Qian, W. A. Henderson, W. Xu, P. Bhattacharya, M. Engelhard, O. Borodin, J. G. Zhang, *Nat. Commun.* **2015**, *6*, 6362; b) D. Cao, X. Sun, Q. Li, A. Natan, P. Xiang, H. Zhu, *Matter* **2020**, *3*, 57–94.
- [23] S. Liu, X. Ji, N. Piao, J. Chen, N. Eidson, J. Xu, P. Wang, L. Chen, J. Zhang, T. Deng, S. Hou, T. Jin, H. Wan, J. Li, J. Tu, C. Wang, *Angew. Chem. Int. Ed. Engl.* **2021**, *60*, 3661–3671.
- [24] a) Y. Gao, T. Rojas, K. Wang, S. Liu, D. Wang, T. Chen, H. Wang, A. T. Ngo, D. Wang, *Nat. Energy* **2020**, *5*, 534–542; b) S. Jiao, X. Ren, R. Cao, M. H. Engelhard, Y. Liu, D. Hu, D. Mei, J. Zheng, W. Zhao, Q. Li, N. Liu, B. D. Adams, C. Ma, J. Liu, J.-G. Zhang, W. Xu, *Nat. Energy* **2018**, *3*, 739–746.
- [25] T. Yang, W. Wang, S. Li, J. Lu, W. Fan, X. Zuo, J. Nan, *J. Power Sources* **2020**, *470*, 228462./DOI: 10.1016/j.jpowsour.2020.228462.
- [26] a) T. Lei, W. Chen, W. Lv, J. Huang, J. Zhu, J. Chu, C. Yan, C. Wu, Y. Yan, W. He, J. Xiong, Y. Li, C. Yan, J. B. Goodenough, X. Duan, *Joule* **2018**, *2*, 2091–2104; b) S. Chen, D. Wang, Y. Zhao, D. Wang, *Small Methods* **2018**, *2*, 1800038; c) P. Li, H. Lv, Z. Li, X. Meng, Z. Lin, R. Wang, X. Li, *Adv. Mater.* **2021**, *33*, 2007803.

- [27] X. Ren, L. Zou, X. Cao, M. H. Engelhard, W. Liu, S. D. Burton, H. Lee, C. Niu, B. E. Matthews, Z. Zhu, C. Wang, B. W. Arey, J. Xiao, J. Liu, J.-G. Zhang, W. Xu, *Joule* **2019**, *3*, 1662–1676.
- [28] a) Y. Chen, W. Zhao, Q. Zhang, G. Yang, J. Zheng, W. Tang, Q. Xu, C. Lai, J. Yang, C. Peng, *Adv. Funct. Mater.* **2020**, *30*, 2000396; b) L. Tan, Y. Sun, C. Wei, Y. Tao, Y. Tian, Y. An, Y. Zhang, S. Xiong, J. Fen, *Small* **2021**, *17*, 2007717.
- [29] a) M. Yoon, Y. Dong, J. Hwang, J. Sung, H. Cha, K. Ahn, Y. Huang, S. J. Kang, J. Li, J. Cho, *Nat. Energy* **2021**, *6*, 362–371; b) G.-L. Xu, Q. Liu, K. K. S. Lau, Y. Liu, X. Liu, H. Gao, X. Zhou, M. Zhuang, Y. Ren, J. Li, M. Shao, M. Ouyang, F. Pan, Z. Chen, K. Amine, G. Chen, *Nat. Energy* **2019**, *4*, 484–494.
- [30] S. Narayan, L. Anand, *J. Electrochem. Soc.* **2020**, *167*, 040525.

Manuscript received: March 25, 2022
Revised manuscript received: April 22, 2022
Version of record online: May 13, 2022
